Materials Advances

ROYAL SOCIETY OF CHEMISTRY

PAPER

View Article Online
View Journal



Cite this: DOI: 10.1039/d5ma00509d

# High-performance hollow microspheres for UV protection from cinnamate-functionalized cellulose nanocrystals and inorganic nanoparticles

Fangyuan Ge, Man-hin Kwok* and To Ngai *

To mitigate the harmful effects of UV radiation, sunscreens are indispensable in sun protection strategies. Sunscreen agents are broadly categorized into two types: inorganic and organic UV filters. Current organic UV filters raise health concerns due to poor photostability and harmful radical generation, while inorganic UV filters often leave white residues on the skin. To address these limitations, we develop a novel method for synthesizing hollow microspheres using cinnamate-functionalized cellulose nanocrystals (Cin-CNCs) and inorganic nanoparticles ($SiO_2$ or $TiO_2$) *via* Pickering emulsion templating to enhance sunscreen performance. The stabilization mechanism involves synergistic interactions between the hydrolysis products of tetraethyl orthosilicate (TEOS), Cin-CNCs, and $SiO_2$ nanoparticles. The resulting cinnamate-functionalized hollow microspheres exhibit excellent water dispersibility and superior photostability compared to traditional organic UV filters. Unlike conventional inorganic UV filters, they display significantly improved transparency in the visible range and enhanced UV shielding properties, owing to the grafting of cinnamate groups and their unique hollow structure. Both Cin-CNCs/$SiO_2$ and Cin-CNCs/$TiO_2$ hollow microspheres demonstrate superior UV protection capabilities compared to their nanoparticles counterparts. When formulated into sunscreens, they achieve higher SPF values than conventional inorganic UV filters. These findings highlight the potential of cinnamate-functionalized hollow microspheres as a next-generation UV-blocking agent in sunscreen formulations.

Received 18th May 2025,
Accepted 1st November 2025

DOI: 10.1039/d5ma00509d

rsc.li/materials-advances



## 1. Introduction

Solar radiation, comprising ultraviolet (UV) (100–400 nm), visible (400–780 nm) and infrared (780–5000 nm) radiation, plays a fundamental role in terrestrial life processes.[1] Moderate solar exposure provides essential benefits, including vitamin D synthesis, cardiovascular health enhancement, and ecological interactions.[2] However, excessive exposure to sunlight, particularly UV radiation, can lead to acute and chronic skin damage, such as sunburn, pigmentation, photoaging, and an elevated risk of photocarcinogenesis.[1,3]

UV radiation is categorized into three distinct spectral regions based on wavelength and biological effects: UVA (320–400 nm), UVB (280–320 nm), and UVC (100–280 nm).[4] UVA radiation primarily activates epidermal melanin, inducing transient pigmentation.[5] In contrast to UVB radiation, these longer wavelength photons penetrate deeper into the dermal layers, causing chronic photodamage manifested as elastosis and wrinkle formation.[5] Moreover, UVA generates reactive oxygen species (ROS) through photochemical interactions with cellular components, leading to oxidative stress and subsequent DNA damage.[6] Although UVB radiation accounts for less than 5% of terrestrial UV exposure, it is primarily responsible for erythema formation through direct chromophore absorption, simultaneously stimulating melanogenesis and epidermal hyperplasia.[5,7] While UVC radiation possesses the highest energy among UV spectra, its complete absorption by atmospheric ozone renders it biologically irrelevant in terrestrial environments.[8]

To counteract the detrimental effects of UV radiation, sunscreens have become indispensable in photoprotection strategies.[9,10] These topical formulations function by absorbing, reflecting, or scattering UV radiation, thereby minimizing its cutaneous penetration.[11] Sunscreen agents are fundamentally categorized into two classes: organic and inorganic UV filters.[9] Organic filters, typically aromatic compounds containing conjugated systems, operate through photon absorption mechanisms.[12] These chemical sunscreens can be further classified based on their spectral coverage: UVA filters (*e.g.*, anthranilates, benzophenones, and dibenzoylmethanes), UVB filters (*e.g.*, cinnamates, salicylates, camphor derivatives,

*Department of Chemistry, The Chinese University of Hong Kong, Shatin, N. T., Hong Kong, P. R. China. E-mail: manhinkwok@cuhk.edu.hk, tongai@cuhk.edu.hk*

and *p*-aminobenzoates), and broad-spectrum filters (*e.g.*, bisoctrizole and silatriazole derivatives).[1,13] Upon UV absorption, the excited state energy is dissipated through thermal relaxation or fluorescence emission, or alternatively drives photochemical transformations.[1,11] While these organic filters offer formulation versatility, enabling precise control over sun protection factor (SPF) and sensory properties,[14] they present several limitations. Photochemical degradation of certain compounds (*e.g.*, avobenzone) necessitates the incorporation of stabilizing additives, thereby increasing formulation complexity and cost.[5] Furthermore, their percutaneous absorption through the stratum corneum and hair follicles raises concerns regarding potential systemic effects, including allergic reactions, photoallergic contact dermatitis,[15] and ecological impacts, particularly their demonstrated toxicity to coral reefs and marine ecosystems (*e.g.*, oxybenzone and octinoxate).[16–19] In contrast, inorganic UV filters, primarily zinc oxide (ZnO) and titanium dioxide ($TiO_2$), offer distinct advantages as physical sunscreens.[20] These particulate materials provide broad-spectrum protection through combined mechanisms of UV absorption, reflection, and scattering, with particular efficacy against UVA radiation.[21,22] While generally exhibiting superior photostability, reduced toxicity, and enhanced safety profiles compared to organic counterparts,[23] their practical application is limited by cosmetic acceptability issues, including visible whitening effects and potential fabric staining. Additionally, the inherent tendency of inorganic nanoparticles to aggregate necessitates surface modification with coating materials (*e.g.*, silicones, fatty acids, or metal oxides such as aluminum, silicon, or zirconium oxides) to ensure adequate dispersion and stability in formulations.[1,24]

To enhance the efficacy and the safety of sunscreens, several innovative strategies have been developed, such as using botanical agents, exploring encapsulation or grafting techniques.[25–28] Botanical agents, comprising secondary metabolites from phototrophic organisms, have evolved sophisticated photoprotective mechanisms through natural selection.[29] Beyond their intrinsic UV-absorbing properties, these phytochemicals demonstrate multifunctional benefits, including potent antioxidant, anti-inflammatory, and immunomodulatory activities, thereby providing comprehensive protection against UV-induced damage.[30] For instance, in regions like Hawaii, botanical sunscreens have replaced synthetic alternatives (*e.g.*, oxybenzone and cinnamates) to prevent coral reef degradation. Certain herbal agents further delay skin aging while maintaining smooth and vibrant skin textures.[31] The growing consumer preference for natural cosmetics has driven the popularity of botanical ingredients in recent years.

Concurrently, nanotechnology has gained prominence in sunscreen formulations, particularly through nanosystems such as nanoemulsions, liposomes, and solid lipid nanoparticles.[32–35] Encapsulating UV filters within these nanosystems improves both efficacy and safety of sunscreen.[33,36,37] A seminal study by Cozzi *et al.*[15] systematically evaluated the cutaneous retention and penetration kinetics of avobenzone and octocrylene in both free and encapsulated forms, while simultaneously assessing their photostability. Their findings revealed that encapsulation technology not only reduces the percutaneous absorption of organic UV filters but also substantially improves their photostability. Parallel advancements in molecular grafting techniques have yielded novel materials with enhanced UV-protective properties. Mendoza *et al.*[38] developed diethyl sinapate-grafted cellulose nanocrystals (CNC-DES), a nanomaterial combining robust UV-blocking capacity with antioxidant activity. The grafting process enhances UV attenuation by cellulose nanocrystals, rendering CNC-DES suitable for sunscreen applications. Additionally, CNC-DES is water-dispersible, biocompatible, light weight, and non-greasy, overcoming key drawbacks of chemical sunscreens such as residue accumulation and environmental toxicity.

While UV filters demonstrate favorable efficacy in sunscreens, commercial formulations often combine multiple filter types to achieve high SPF or broad-spectrum coverage.[39] When employed individually, inorganic filters require substantially higher concentrations for comparable efficacy. For instance, achieving SPF 30 in lotion formulations demands ZnO concentrations exceeding 20–25 wt%. Additionally, the high refractive indices of $TiO_2$ and ZnO induce light-scattering effects, resulting in a pronounced white cast on the skin.[40] In contrast, organic UV filters exhibit superior UV absorption capacity but suffer from limited photostability, thus necessitating the incorporation of stabilizing additives (*e.g.*, antioxidants or photostabilizers) within formulations.

To address these challenges, we developed an innovative approach to create a novel UV filter system that combines broad-spectrum protection (UVA-UVB) with enhanced photostability. In this work, we synergized the merits of organic and inorganic UV filters by engineering hollow microspheres *via* Pickering emulsion templating, co-stabilized by cinnamate-functionalized cellulose nanocrystals (Cin-CNCs) and inorganic nanoparticles ($SiO_2$ or $TiO_2$). The cinnamate motif was strategically selected as the organic UVB absorber not only for its characteristically strong absorption in the UVB region, attributable to the conjugated system of the benzene ring and the adjacent carbon–carbon double bond, but also for its molecular compatibility with the robust esterification chemistry used for CNC functionalization. Cinnamate groups exhibit strong UVB absorption due to the conjugated structure of the benzene ring and adjacent carbon double bonds. However, most cinnamate derivatives are hydrophobic and undergo photodimerization upon UV irradiation (wavelength $\lambda > 280$ nm).[25] Our approach directly addresses these drawbacks: grafting cinnamate groups onto the hydrophilic and rigid CNC backbone significantly improves their photostability through introduced steric hindrance that suppresses photodimerization, while concurrently converting them into a particulate emulsifier. Subsequent assembly into hydrophilic hollow microspheres further enhances their water dispersibility and minimizes the risk of skin penetration.[25] Furthermore, the hollow architecture amplifies UV attenuation through synergistic reflection and scattering at light-refractive interfaces, while incorporating $SiO_2$ or $TiO_2$ nanoparticles extends UVA protection *via* complementary absorption mechanisms and reinforces the microspheres' mechanical

robustness. These Cin-CNC-based hollow microspheres demonstrated superior UV-shielding efficacy and photostability, offering a streamlined solution for sunscreen formulations by minimizing reliance on multiple organic components.

## 2. Experimental

### 2.1. Materials

CNCs were purchased from ScienceK New Material Technology Co., Ltd, China. Hydrophobic fumed silica (R974, hydrophobized by dichlorodimethylsilane) with an average primary particle size of 16 nm was donated by Evonik Industries AG, Germany. Hydrophobic $TiO_2$ nanoparticles (TX-85, $TiO_2$ purity: 80%, surface-modified with silica and dimethicone) with an average primary particle size of 30 nm were purchased from Sunjin Company, Korea. 4-Dimethylaminopyridine (DMAP) and triethylamine (TEA) were obtained from International Laboratory (USA) and Scharlau (Spain), respectively. Cinnamoyl chloride and sodium hydroxide were sourced from Macklin and Aladdin. Tetraethyl orthosilicate (TEOS) and dodecane were purchased from Sigma-Aldrich. Deionized water (18.2 MΩ) was produced using a Milli-Q system and used in all experiments.

### 2.2. Synthesis of Cin-CNCs

Cin-CNCs were synthesized following a previously reported method with modifications.[25] Briefly, CNCs (1 g) were dispersed in DMF (80 mL) under ultrasonication. Subsequently, TEA (2.58 mL, 18.5 mmol) and DMAP (1.13 g, 9.3 mmol) were added to the dispersion and stirred for 30 min.[41] The mixture was cooled in an ice bath, followed by dropwise addition of a cinnamoyl chloride solution (3.33 g, 20 mmol in 20 mL DMF). The reaction was allowed to proceed at room temperature for 24 h. The resulting Cin-CNCs were purified *via* three cycles of centrifugation in DMF, followed by dialysis against deionized water for 7 days. Freeze-drying was employed to remove residual water, yielding the final Cin-CNCs. The grafting fraction of cinnamate groups was controlled by adjusting the mass ratio of CNCs to cinnamoyl chloride. A schematic illustration of the synthesis process is provided in Fig. 1B.

### 2.3. Fabrication of the O/W Pickering emulsion templates and hollow microspheres

Hollow microspheres were fabricated *via* an emulsion templating approach. Cin-CNCs (0.02 g) were dispersed in 4 mL of deionized water (0.5 wt%) using an ultrasonic cell disruptor (Ningbo Xin Zhi Biotechnology Co.). Subsequently, 1 mL of dodecane containing 50% tetraethyl orthosilicate (TEOS) was mixed with 4 mL of the Cin-CNC aqueous dispersion (pH 10.5) to achieve an oil-to-water volume ratio of 1 : 4. The mixture was homogenized at 10 000 rpm for 30 s using a high-pressure homogenizer, followed by ultrasonication at 400 W for 2 min (5 s on, 5 s off) to form O/W Pickering emulsion templates. Throughout the process, an ice bath was applied to maintain thermal control. The emulsion was incubated at 65 °C for 24 h to facilitate interfacial polymerization. The product was washed three times with ethanol and dialyzed against deionized water for 5 days. Finally, hollow microspheres were obtained by freeze-drying to remove residual water. A schematic representation of the preparation process is illustrated in Fig. 1C.

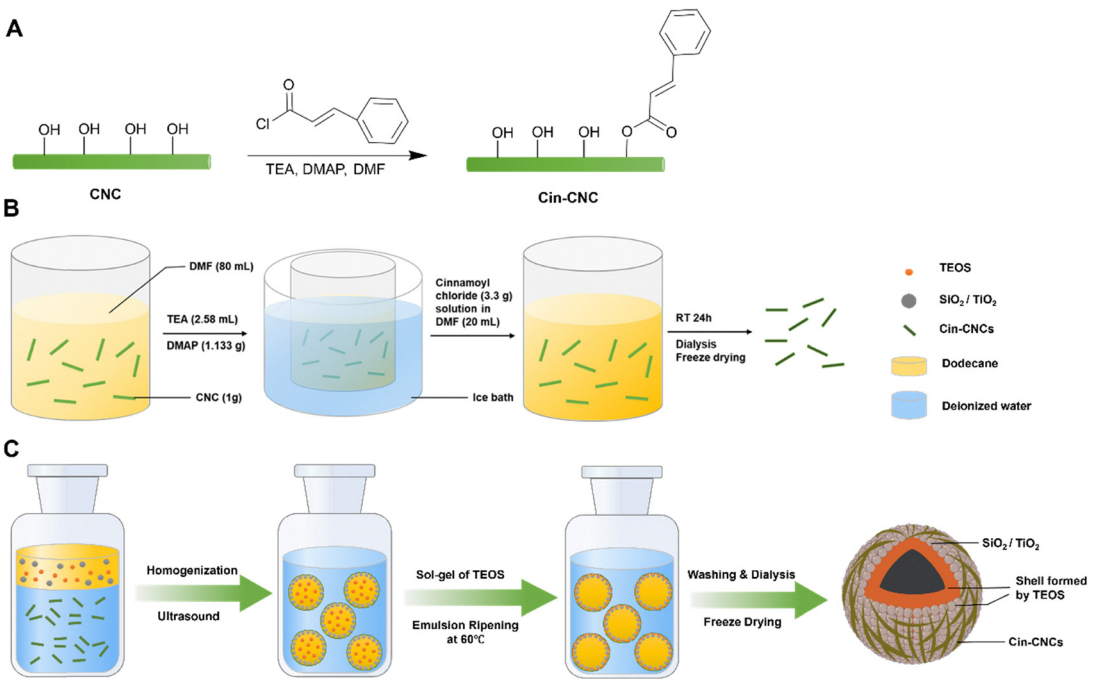


Fig. 1 (A) Synthesis of a Cin-CNCs-based Pickering emulsifier *via* acylation of cellulose nanocrystals (CNCs) with cinnamoyl chloride; (B) schematic of the synthetic route for Cin-CNCs. (C) Formation mechanism of hollow microspheres co-stabilized by Cin-CNCs and $SiO_2$ (or $TiO_2$) nanoparticles.

### 2.4. Characterization

**2.4.1. Fourier transform infrared (FTIR) spectroscopy.** The successful grafting of cinnamate groups on CNCs was confirmed by Fourier-transform infrared (FTIR) spectroscopy (Nicolet iS10, Thermo Scientific, USA). Freeze-dried samples were ground with potassium bromide (KBr) in an agate mortar and pressed into translucent pellets. FTIR spectra were recorded in the wavenumber range of 4000–400 $cm^{-1}$.

**2.4.2. Transmission electron microscopy (TEM).** The size, morphology of Cin-CNCs, and microstructure of hollow microspheres were characterized by transmission electron microscopy (TEM). TEM images were acquired using a Tecnai G2 Spirit Bio microscope (FEI Company, USA) operated at an acceleration voltage of 120 kV. For sample preparation, a droplet of aqueous dispersion ($1 \times 10^{-4}$ g $mL^{-1}$) was deposited onto carbon-coated copper grids *via* drop-casting and air-dried overnight at room temperature.

**2.4.3. Scanning electron microscopy with energy dispersive X-ray spectroscopy (SEM-EDX).** The size and morphology of hollow microspheres were characterized using SEM (Quanta 400 F, FEI Company, USA) equipped with a field emission electron gun at 10 kV. Energy-dispersive X-ray spectroscopy (EDX) was employed to analyze elemental composition. Aqueous dispersions of hollow microspheres ($5 \times 10^{-4}$ g $mL^{-1}$) were drop-cast onto silicon wafers and air-dried overnight at 25 °C.

**2.4.4. Optical microscope.** An optical microscope (OLYMPUS, Japan) was used to capture the morphology of Pickering emulsion templates at 10 and 40 magnifications in the bright-field modes at 25 °C.

**2.4.5. Size measurements of hollow microspheres.** The particle size distribution was statistically analyzed by measuring the diameters of over 200 hollow microspheres from three independent SEM images per sample using ImageJ software (Version 1.53t, National Institutes of Health, USA).

**2.4.6. ζ-Potential measurements.** The ζ-potentials of CNCs and Cin-CNCs ($1 \times 10^{-4}$ g $mL^{-1}$) were measured using a Zetasizer Nano ZS90 (Malvern Panalytical, UK). Reported values represent the average of three consecutive measurements, with each measurement consisting of 10 automatic runs.

**2.4.7. Three-phase contact angle measurements.** The wettability of CNC-based particles was quantified through water-in-air three-phase contact angle measurements using a contact angle goniometer (OCA 25, DataPhysics Instruments, Germany). Thin films of CNCs and Cin-CNCs were prepared by spin-coating aqueous dispersions ($5 \times 10^{-3}$ g $mL^{-1}$) onto silicon wafers. After complete solvent evaporation, a 3.0 μL droplet of deionized water was deposited on the coated surface. Contact angles were averaged from three independent measurements per sample.

**2.4.8. Cinnamate grafting fraction quantification.** The grafting fraction of cinnamate groups on the surface of CNCs was quantified using ultraviolet-visible (UV-vis) spectroscopy (UV-3600 Plus, Shimadzu, Japan). Absorbance spectra of CNC (blank) and Cin-CNC dispersions ($4 \times 10^{-5}$ g $mL^{-1}$ in DMF) were recorded at 278 nm. The grafting fraction $\phi$ (defined as the percentage of hydroxyl groups substituted by cinnamate moieties) was calculated *via* eqn (1), with derivation detailed in SI Section S4:

$$\phi = \frac{100(A_{\text{Cin-CNC}} - A_{\text{CNC}})}{302 - 39(A_{\text{Cin-CNC}} - A_{\text{CNC}})} \quad (1)$$

**2.4.9. Hydrodynamic stability assessment.** Aqueous dispersions of Cin-CNCs or hollow microspheres ($1 \times 10^{-3}$ g $mL^{-1}$) were allowed to sediment under gravity. Time-dependent turbidity changes were documented photographically at predefined intervals (0, 1, 3, 6, and 24 h). Colloidal stability was comparatively analyzed based on sedimentation kinetics and supernatant clarity.

**2.4.10. Photochemical stability analysis.** The Cin-CNCs/$SiO_2$ hollow microsphere dispersions were subjected to UV-A irradiation (365 nm) using a XM210 UV-LED system (Aventk, China; irradiance: 130 mW $cm^{-2}$, equivalent to 1.3× solar UV intensity). UV-vis spectral evolution was monitored at 278 nm to track photo-dimerization kinetics through cyclobutane formation.

**2.4.11. UV-shielding performance evaluation.** UV-vis-NIR transmission spectra (280–800 nm) were recorded using a UV-3600 Plus spectrometer. UV-blocking efficiency was quantified by transmittance suppression in the 280–400 nm range, while visible transparency was assessed *via* 400–800 nm transmission profiles.

**2.4.12. *In vitro* SPF evaluation.** SPF values were determined using an SPF-290AS Automated Analyzer (Solar Light, USA) following ASTM E3073-22 guidelines.[19] Samples were uniformly coated on 3M Transpore® tape-laminated quartz slides (2 layers, 19 × 35 mm) and equilibrated in darkness for 20 min. Corrected transmittance spectra (290–400 nm, 1 nm resolution) were obtained by subtracting substrate baselines. SPF values were computed *via* integrated erythemal effectiveness weighting.

## 3. Results and discussion

### 3.1. Synthesis and characterization of Cin-CNCs

The acylation of CNCs with cinnamoyl chloride was performed using TEA and DMAP as catalysts.[41] The synthetic procedure of Cin-CNCs is illustrated schematically in Fig. 1B. TEM analysis revealed that the esterification reaction did not disrupt the needle-like morphology of CNCs, as demonstrated in Fig. 2A and B. Based on TEM measurements, the average particle dimensions were calculated to be 168.5 ± 18.6 nm in length and 6.1 ± 2.8 nm in width. Successful grafting of cinnamate groups onto the CNC surface was confirmed by FTIR spectroscopy, which identified characteristic vibration bands at 1719.301 $cm^{-1}$ (carboxyl C═O stretching), 1635.409 $cm^{-1}$ (alkene C═C stretching), and 769.491 $cm^{-1}$ (aromatic C–H out-of-plane bending), as shown in Fig. 2C.[25]

The grafting fraction of cinnamate groups was quantified using UV-visible spectroscopy. A calibration curve was established to correlate the maximum absorbance with cinnamoyl chloride concentration, as described by eqn (2) (Fig. S2A). Cin-$CNC_n$ samples were prepared by varying the mass ratio of CNCs

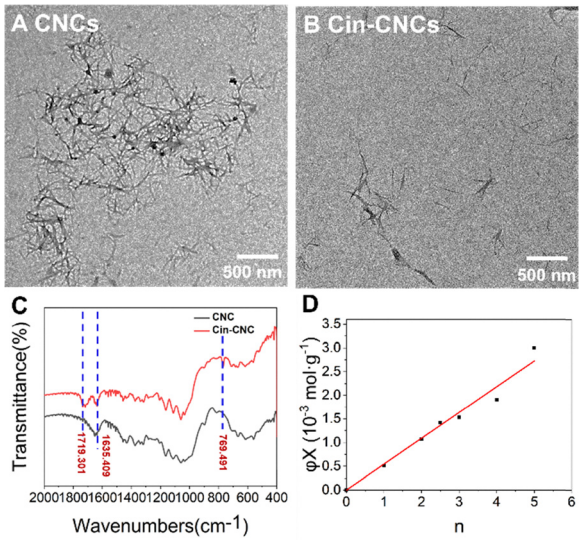


Fig. 2 TEM images of (A) pristine CNCs and (B) Cin-CNCs. (C) FTIR spectra of pristine CNCs and Cin-CNCs synthesized at a weight ratio of CNCs to cinnamoyl chloride of 2 : 5. (D) Correlation between the parameter "$n$" and the grafting fraction "$\phi X$".

Table 1 Grafting fractions of Cin-CNCs with varying mass ratios of CNCs to cinnamoyl chloride

| | $A_{\text{Cin-CNC}} - A_{\text{CNC}}$ | $\phi$ | $\phi X$/mol g$^{-1}$ |
|---|---|---|---|
| Cin-CNC$_1$ | 0.48 | 0.1695 | $5.08 \times 10^{-4}$ |
| Cin-CNC$_2$ | 0.946 | 0.3570 | $1.07 \times 10^{-3}$ |
| Cin-CNC$_{2.5}$ | 1.205 | 0.4728 | $1.42 \times 10^{-3}$ |
| Cin-CNC$_3$ | 1.287 | 0.5113 | $1.53 \times 10^{-3}$ |
| Cin-CNC$_4$ | 1.535 | 0.6342 | $1.90 \times 10^{-3}$ |
| Cin-CNC$_5$ | 2.189 | 1 (defined) | $3.00 \times 10^{-3}$ |

to cinnamoyl chloride ($1 : n$). The UV absorbance of a blank CNC suspension and Cin-CNCs ($4 \times 10^{-5}$ g mL$^{-1}$) was measured (Fig. S2B). Based on the absorbance of fully grafted Cin-CNC5, it was determined that 1 g of CNCs provides $3 \times 10^{-3}$ mol of reaction sites, enabling the quantification of cinnamate groups grafted per gram of CNCs (Table 1). The linear relationship between the parameter "$n$" and the grafting fraction "$\phi X$" is depicted in Fig. 2D and mathematically expressed in eqn (3).

$$y = 152\,257x \quad (2)$$

$$\phi X = 0.5451n \quad (3)$$

The hydrodynamic stability and hydrophobicity of Cin-CNCs, synthesized with varying grafting fractions, exhibited significant variations. These properties are critical when evaluating their potential as particle emulsifiers. Pristine CNCs are inherently hydrophilic and readily disperse in water due to the presence of abundant hydroxyl and sulfate ester groups. In contrast, Cin-CNCs demonstrated reduced hydrophilicity owing to the grafting of hydrophobic cinnamate groups. Although Cin-CNCs could be dispersed in water through homogenization, their aqueous

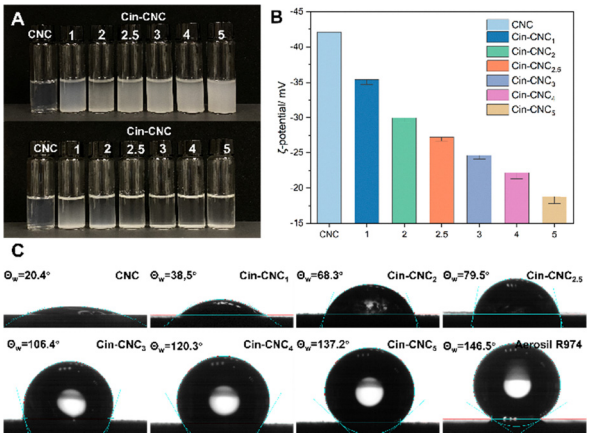


Fig. 3 (A) Optical images of CNC and Cin-CNC dispersions ($1 \times 10^{-3}$ g mL$^{-1}$) in water immediately after preparation and after 2 hours. (B) Zeta potentials of CNCs and Cin-CNCs with different grafting fractions at identical pH values. (C) Contact angles of $SiO_2$ nanoparticles (Aerosil R974), CNCs, and Cin-CNCs with varying grafting fractions.

dispersions appeared opaque and exhibited gradual sedimentation, as shown in Fig. 3A. The zeta potentials of CNCs and Cin-CNCs with different grafting fractions (measured at identical pH values) are presented in Fig. 3B. The surface charge of Cin-CNCs was modulated by both the chemical modification and the grafting fraction of cinnamate groups, which collectively influenced their colloidal stability and aggregation behaviour. To further assess the impact of cinnamate grafting on surface wettability, contact angle measurements were conducted. The results, summarized in Fig. 3C, confirmed that the hydrophobic modification of CNCs significantly increased their contact angle, with higher grafting fractions leading to greater hydrophobicity.

### 3.2. Fabrication and properties of hollow microspheres

Hollow microspheres were fabricated using oil-in-water Pickering emulsion templates. The emulsifier particles surrounding the droplets were immobilized through the cross-linking of TEOS silica precursors at the oil–water interface, as illustrated in Fig. 1C.

**3.2.1. Structural features of hollow microspheres.** SEM images of the Cin-CNCs/$SiO_2$ hollow microspheres revealed a rough surface and a well-preserved spherical morphology (Fig. 4A), with a distinct hollow structure (Fig. 4B). The distribution of particulate emulsifiers within the microsphere shell was preliminarily observed *via* TEM (Fig. 4C). The dark gray particles, approximately 13 ± 1.2 nm in size, were identified as $SiO_2$ nanoparticles (Aerosil R974), consistent with their individual dispersion observed in TEM (Fig. 4D). Due to the extensive cross-linked network formed by hydrolysis products of TEOS and the relatively low contrast of Cin-CNCs compared to $SiO_2$ nanoparticles under TEM imaging, the presence of Cin-CNCs was obscured in TEM images. To confirm their incorporation, EDX analysis was conducted. Fig. 4E displays the SEM images of the hollow microspheres alongside the corresponding elemental mappings for carbon (red), oxygen (green), and silicon (blue). The samples were placed on a silicon

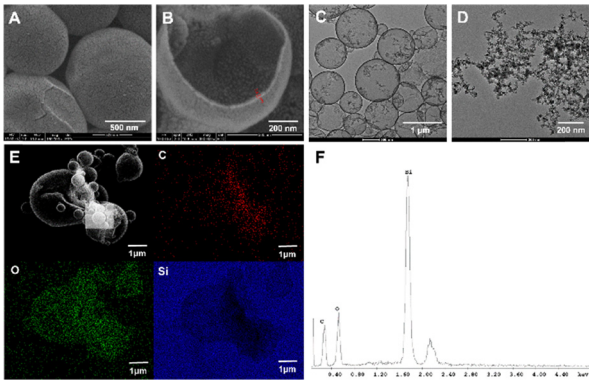


Fig. 4 (A) and (B) SEM images and (C) TEM images of Cin-CNCs/$SiO_2$ hollow microspheres. (D) TEM images of $SiO_2$ nanoparticles (Aerosil R974). (E) EDX elemental scanning and mapping, and (F) EDX spectrum plots of Cin-CNCs/$SiO_2$ hollow microspheres.

wafer for analysis, resulting in a strong silicon signal. However, since this signal did not interfere with the analysis, the EDX spectra were not calibrated by subtracting the background signal of a blank silicon wafer. Based on the results shown in Fig. 4E and F, the presence of the carbon EDX signal is confirmed. Since the hollow microspheres were thoroughly dialyzed and dried, residual organic compounds were negligible, and the carbon signal could be exclusively attributed to Cin-CNCs.

**3.2.2. Pickering emulsion template stabilization mechanisms.** The stabilization mechanisms of Pickering emulsion templates and interfacial interactions between emulsifiers were systematically investigated prior to microsphere shell formation. Upon combining TEOS with aqueous phase at pH 10.5, controlled hydrolysis generated silanol intermediates (Si-OH) through partial ethoxyl group cleavage. Although native TEOS exhibits inherent hydrophobicity due to its non-polar ethoxysilane structure, the partial hydrolysis of 1–3 ethoxyl groups induces a critical structural transformation. This process introduces hydrophilic hydroxyl groups while retaining sufficient hydrophobic moieties, thereby enhancing the amphiphilic character and interfacial activity of the resulting ethoxyl silanols.

To confirm the role of silanols (partial hydrolysis product of TEOS) in stabilizing Pickering emulsion templates, three control emulsions were prepared: (1) deionized water/dodecane (emulsion I), (2) deionized water/dodecane with 50% TEOS under unadjusted pH (emulsion II), and (3) the same system at pH 10.5 (emulsion III). As shown in Fig. 5A, neither the pure dodecane/water system (Fig. 5A-I) nor the TEOS-containing system at neutral pH (Fig. 5A-II) formed stable emulsions. Although TEOS addition slightly increased oil phase polarity, insufficient hydrolysis under neutral conditions prevented silanol generation. In contrast, alkaline conditions (pH 10.5) enabled TEOS hydrolysis to produce surface-active silanols, yielding transient emulsion stability (Fig. 5A-III). However, this emulsion destabilized within 24 h due to subsequent TEOS polycondensation into non-surface-active silicic acid and silica.

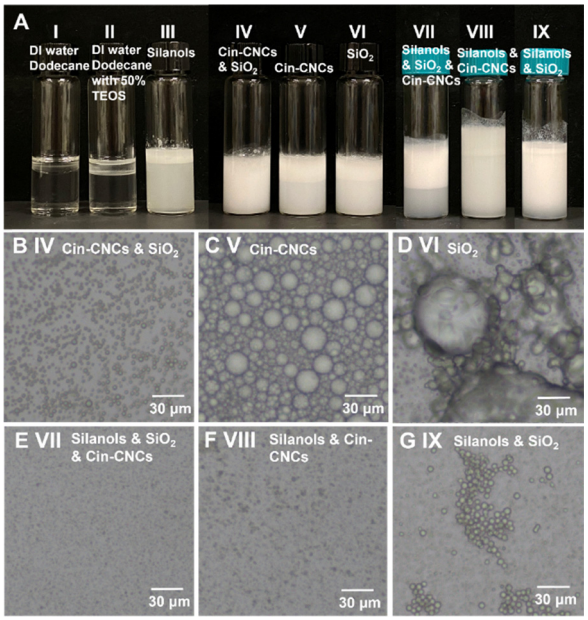


Fig. 5 (A) Appearance and (B)–(G) optical microscope images of emulsions stabilized by: (I) no Pickering emulsifier (deionized water/dodecane); (II) no Pickering emulsifier (deionized water/dodecane with 50% TEOS under unadjusted pH conditions); (III) silanols; (IV) Cin-CNCs and $SiO_2$ nanoparticles; (V) Cin-CNCs; (VI) $SiO_2$ nanoparticles; (VII) silanols, Cin-CNCs, and $SiO_2$ nanoparticles; (VIII) silanols and Cin-CNCs; (IX) silanols and $SiO_2$ nanoparticles. The pH of the water phase for emulsions 4–9 was adjusted to 10.5.

Comparative analysis of emulsion stabilization mechanisms revealed synergistic effects. Emulsions stabilized solely by $SiO_2$ nanoparticles (emulsion 5, Fig. 5D) exhibited larger, irregular droplets, while co-stabilization with silanols (emulsion 8, Fig. 5G) produced smaller, more uniform droplets. This indicates that silanols and $SiO_2$ nanoparticles synergistically enhance emulsion stability through complementary interfacial interactions. Similar synergy was observed between silanols and Cin-CNCs (Fig. 5C *vs.* Fig. 5F), where silanols likely occupied interfacial regions uncoated by Cin-CNCs, further reducing interfacial tension. Furthermore, co-stabilization by Cin-CNCs and $SiO_2$ nanoparticles (Fig. 5B–D) demonstrated improved emulsion uniformity compared to individual components, suggesting cooperative adsorption at the oil–water interface. Optimal stabilization was achieved in ternary systems (silanols/Cin-CNCs/$SiO_2$, Fig. 5E), where hierarchical component arrangement yielded the smallest and most homogeneous droplets, conclusively demonstrating tripartite synergy.

Building upon these observations, we propose a more detailed mechanism for the interfacial interactions and their contribution to the long-term stability of the precursor emulsions and the resulting hollow microspheres. The silanol intermediates, acting as molecular surfactants, are posited to reduce the interfacial tension and facilitate the initial formation of fine droplets. Concurrently, the Cin-CNCs and $SiO_2$ nanoparticles, as solid Pickering stabilizers, adsorb irreversibly at the oil–water interface, providing a robust mechanical barrier against coalescence. The enhanced stability in ternary

systems suggests that the silanols may act as 'interfacial glue', potentially forming hydrogen bonds or other polar interactions with the hydroxyl groups on both the Cin-CNCs and the $SiO_2$ nanoparticles. This cooperative interaction likely leads to the formation of a densely packed and coherent interfacial film, as evidenced by the smallest droplet size achieved (Fig. 5E). This consolidated interface is crucial, as it serves as the direct template for the subsequent formation of the hollow microsphere shell *via* TEOS condensation. The robustness of this initial composite interface directly translates into the improved mechanical integrity and structural uniformity of the final hollow microspheres, as observed by SEM (Fig. 4A and B).

**3.2.3. Effect of the Cin-CNCs grafting fractions on hollow microspheres.** The structural evolution of hollow microspheres was systematically investigated as a function of Cin-CNC surface modification. Six Cin-CNC variants with progressively increasing grafting degrees (0.17–1.00) were synthesized alongside pristine CNCs, maintaining constant $SiO_2$ nanoparticle content (Table S1).

The morphological characteristics and size distributions of hollow microspheres were systematically analyzed through SEM imaging (Fig. 6A–G) and particle size analysis (Fig. 7G and J). Progressive enhancement in mechanical stability and size uniformity was observed with increasing grafting fractions of hydrophilic Cin-CNCs (0.17–0.47, Fig. 6A–D). This improvement arises from the optimized balance between two competing interfacial interactions: (1) gradual reduction in Cin-CNCs' surface charge magnitude (as evidenced by zeta potential measurements) decreased electrostatic repulsion with $SiO_2$ nanoparticles, facilitating cooperative interfacial assembly. (2) Controlled hydrophobization improved interfacial activity compared to pristine CNCs, which exhibited excessive hydrophilicity for effective Pickering stabilization. Beyond the critical grafting fraction of 0.47, structural degradation became evident (Fig. 6E–G), manifesting as fragmented morphologies post-processing. This transition correlates with contact angle inversion ($>90^\circ$) and diminished electrostatic screening between components, ultimately destabilizing the emulsion template. Optimal performance was achieved at 0.47 grafting fraction, yielding microspheres with enhanced size homogeneity and mechanical integrity through synergistic stabilization with $SiO_2$ nanoparticles.

**3.2.4. Effect of Cin-CNCs or $SiO_2$ nanoparticle concentration on hollow microspheres.** The concentration effects of $SiO_2$ nanoparticles were systematically investigated through SEM characterization. In the absence of $SiO_2$ nanoparticles (Fig. 7A), the resulting hollow microspheres exhibited structural fragility and irregular morphology. Progressive addition of $SiO_2$ nanoparticles (Fig. 7B–D) enhanced both mechanical stability and size uniformity, as corroborated by particle size distribution analyses (Fig. 7H and K). This improvement can be attributed to two synergistic mechanisms: (1) increased nanoparticle loading enhanced the emulsion template stability through improved interfacial coverage, and (2) reinforced

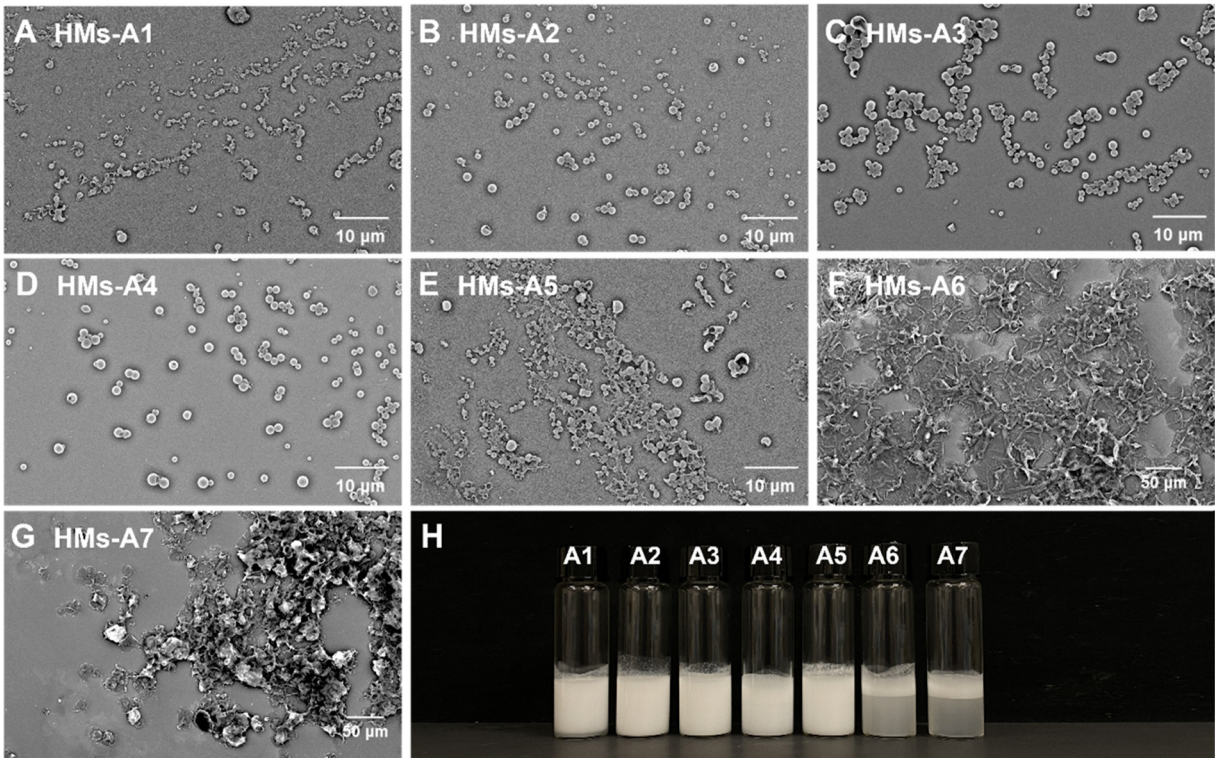


Fig. 6 (A)–(G) SEM images and (H) appearance photos of Cin-CNCs/$SiO_2$ hollow microspheres prepared using pristine CNCs (A1) and Cin-CNCs with six different grafting fractions (A2: 0.17; A3: 0.36; A4: 0.47; A5: 0.51; A6: 0.63; A7: 1.00) and equal amounts of $SiO_2$ nanoparticles (refer to Table S1 for more details).

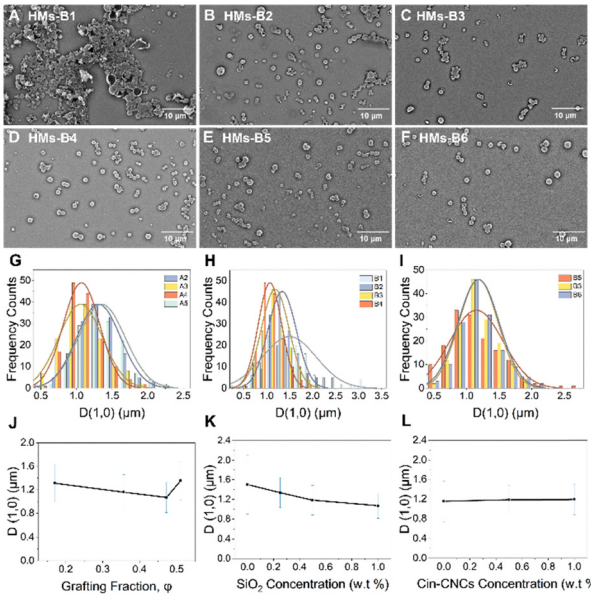


Fig. 7 (A)–(F) SEM images of Cin-CNCs (grafting fraction: 0.47)/$SiO_2$ hollow microspheres prepared with different Cin-CNCs and $SiO_2$ concentrations (refer to Table S1 for more details of samples). Distribution of the number-average diameter *D* (1,0) of the hollow microspheres obtained at different grafting fractions of Cin-CNCs (G), different concentrations of $SiO_2$ nanoparticles (H), and different concentrations of Cin-CNCs (I). Evolution of the number-average diameter *D* (1,0) and size dispersity ($\sigma$) as a function of grafting fractions of Cin-CNCs (J), different concentrations of $SiO_2$ nanoparticles (K), and different concentrations of Cin-CNCs (L).

shell formation *via* nanoparticle accumulation at the oil–water interface.

Similarly, varying Cin-CNCs concentration demonstrated significant morphological control (Fig. 7C, E and F). Optimal Cin-CNCs loading yielded microspheres with enhanced structural integrity and reduced size polydispersity (Fig. 7I and L). However, beyond this critical concentration, additional Cin-CNCs failed to further improve microsphere quality. This saturation behaviour suggests limited available adsorption sites at the oil–water interface, consistent with the finite interfacial area predicted by Pickering emulsion theory.

**3.2.5. Hydrodynamic stability of hollow microspheres.** The hydrodynamic stability of UV filters critically determines their applicability in waterborne sunscreens. To evaluate this property, sedimentation behaviour was analyzed through static settling tests. As shown in Fig. S4A, pristine Cin-CNCs required sonication for aqueous dispersion and formed opaque suspensions. In contrast, Cin-CNCs/$SiO_2$ hollow microspheres spontaneously dispersed in water without external energy input, forming translucent suspensions. This disparity intensified over time: Cin-CNCs completely sedimented within 1 hour (Fig. S4B), whereas the hollow microspheres maintained colloidal stability. Furthermore, the hybrid microspheres demonstrated dual-phase compatibility, exhibiting stable dispersion in both aqueous and lipophilic media (caprylic/capric triglycerides, Fig. S4C). This biphasic dispersibility surpasses the performance of individual components, highlighting the structural advantages of the hollow architecture for cosmetic formulations.

**3.2.6. Photostability of hollow microspheres.** The photostability of UV filters is a critical parameter for practical applications. Cinnamate groups are known to undergo [2π + 2π] photodimerization upon exposure to UV radiation ($\lambda > 280$ nm), as evidenced by changes in the UV absorption band associated with the π–π* electronic transition of the conjugated C=C bond.[25] To evaluate photostability, Cin-CNCs/$SiO_2$ hollow microspheres were irradiated at 365 nm using a UV-LED curing machine (130 mW $cm^{-2}$, comparable to terrestrial solar irradiance). As shown in Fig. S3, the characteristic absorption peak at 278 nm gradually decreased with irradiation time, consistent with photodimerization kinetics. Remarkably, the hollow microspheres retained 94.91% of their initial absorbance after 5 h of continuous UV exposure, demonstrating exceptional photostability. This performance surpasses that of conventional cinnamate derivatives,[42] which we attribute to two synergistic effects: (1) steric hindrance imposed by the CNC matrix, and (2) UV shielding provided by the $SiO_2$ shell.

**3.2.7. Cin-CNCs/$TiO_2$ hollow microspheres.** In this study, $TiO_2$ nanoparticles (Sunjin Company) with a $SiO_2$ surface coating were employed. Given their structural similarity to $SiO_2$ nanoparticles, we hypothesize that they stabilize Pickering emulsions through analogous mechanisms. To validate the universality of this stabilization approach, hydrophobic $TiO_2$ nanoparticles (diameter ≈ 25 nm) were substituted for $SiO_2$ nanoparticles in hollow microsphere fabrication (Fig. 8D). Using Cin-CNCs with an optimized grafting fraction (0.47), the resulting $TiO_2$-based microspheres (Fig. 8B) exhibited morphological characteristics comparable to their $SiO_2$ counterparts,

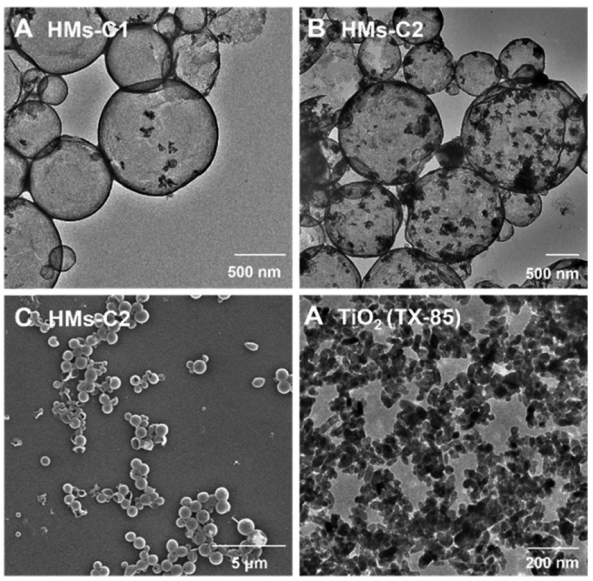


Fig. 8 (A) TEM images of CNCs/$TiO_2$ hollow microspheres. (B) TEM images of Cin-CNCs/$TiO_2$ hollow microspheres. (C) SEM images of Cin-CNCs/$TiO_2$ hollow microspheres. (D) TEM images of $TiO_2$ nanoparticles (refer to Table S1 for more details).

confirming the generalizability of this emulsion templating strategy. This model is readily amenable to the incorporation of other functional inorganic nanoparticles, most notably ZnO. The integration of ZnO into this hollow microsphere architecture represents a highly promising future direction, which is anticipated to further augment the UVA protection performance of the system while leveraging the established advantages of the hollow structure and organic–inorganic synergy.

**3.2.8. UV-shielding properties of hollow microspheres.** Fig. 9 compares the UV-shielding performance of Cin-CNCs/$SiO_2$ and Cin-CNCs/$TiO_2$ hollow microspheres. Consistent with the findings in Sections 3.2.3 and 3.2.4, Cin-CNCs/$SiO_2$ hollow microspheres with a grafting fraction of 0.47 exhibited optimal UV-blocking efficiency across the UV spectrum (Fig. 9A). Enhanced UV-shielding capability was achieved through increased Cin-CNCs concentration and compositional ratio (Fig. 9B). Substitution of $SiO_2$ with $TiO_2$ nanoparticles significantly improved UV attenuation, particularly in the UVB range (280–320 nm). However, this enhancement coincided with reduced visible light transmittance (380–760 nm), as evidenced by the spectral profiles shown in Fig. 9D. Notably, Cin-CNCs/$SiO_2$ hollow microspheres demonstrated complete UVB blockage at a critical concentration of $2 \times 10^{-4}$ g $mL^{-1}$, establishing their potential for full-spectrum UV protection applications.

**3.2.9. *In vitro* SPF evaluation.** To simulate real sunscreens, blank creams were prepared according to the formulation (Table S2), along with creams containing 5 wt% of different types of UV filters. The *in vitro* SPF of the hollow microspheres was then determined. Samples (2 mg $cm^{-2}$) were applied to a 3M Transpore® tape (two layers, 19 mm × 35 mm) attached to a quartz slide. The slide with the samples was placed in the dark and dried for 20 minutes prior to measurement. The results are shown in Table 2.

When the cream was dispersed with 5 wt% Cin-CNCs/$SiO_2$ hollow microspheres, the SPF value reached 4.51 ± 0.71, while

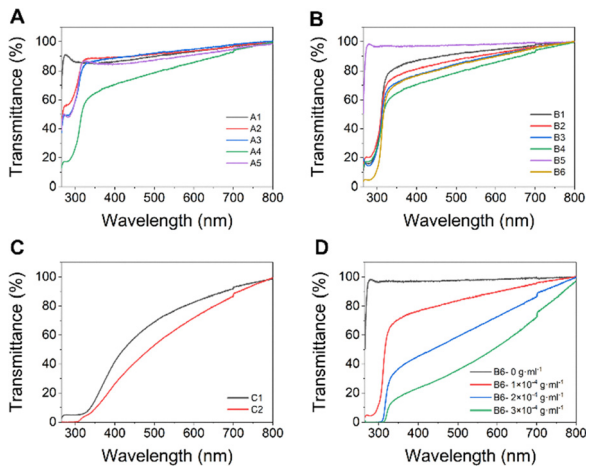


Fig. 9 (A) and (B) UV-vis transmittance spectra of Cin-CNCs/$SiO_2$ hollow microspheres. (C) UV-vis transmittance spectra of Cin-CNCs/$TiO_2$ hollow microspheres (the concentration of hollow microspheres was $1 \times 10^{-4}$ g $mL^{-1}$). (D) Effect of the Cin-CNCs/$SiO_2$ hollow microsphere concentration on the optical transmittance at different UV wavelengths.

Table 2 SPF evaluation results of different samples

| Samples | SPF |
|---|---|
| Blank cream | 0.99 ± 0.01 |
| Cream with 5 wt% Aerosil R974 | 1.10 ± 0.04 |
| Cream with 5 wt% TX-85 | 3.92 ± 0.44 |
| Cream with 5 wt% Cin-CNCs/$SiO_2$ HMs (B6) | 4.51 ± 0.71 |
| Cream with 5 wt% Cin-CNCs/$TiO_2$ HMs (C2) | 5.35 ± 0.74 |
| Sunscreen with 15 wt% TX-85 | 10.73 ± 1.77 |
| Sunscreen with 10 wt% TX-85 and 5 wt% Cin-CNCs/$SiO_2$ HMs (B6) | 11.28 ± 1.86 |
| Sunscreen with 10 wt% TX-85 and 5 wt% Cin-CNCs/$TiO_2$ HMs (C2) | 13.41 ± 1.80 |

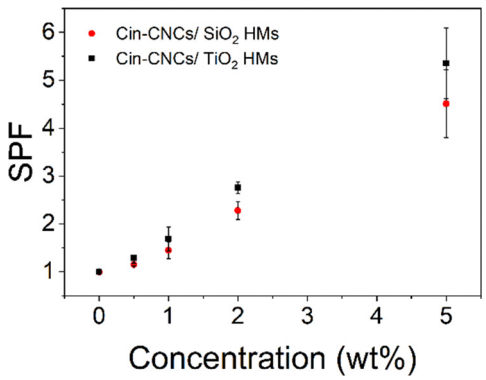


Fig. 10 Variation of the SPF value of cream with the concentration of added hollow microspheres.

the cream dispersed with 5 wt% Cin-CNCs/$TiO_2$ hollow microspheres had an SPF value of 5.35 ± 0.74. For the $SiO_2$-based microspheres, the significant increase in the SPF value was attributed to the grafted cinnamate groups on the CNC surface of the hollow microspheres. In contrast, the improvement in the SPF value for the $TiO_2$ hollow microspheres compared to solid $TiO_2$ was less pronounced, as $TiO_2$ nanoparticles alone provide substantial UV protection. Nevertheless, the Cin-CNCs/$TiO_2$ hollow microspheres still enhanced SPF performance, with their UVB-blocking ability significantly improved compared to pure inorganic UV filters. Additionally, both types of Cin-CNC/inorganic nanoparticle hollow microspheres exhibited UVA protection capabilities, indicating a broader spectrum of UV protection. The relationship between the SPF value of the cream and the concentration of added hollow microspheres is summarized in Fig. 10. The SPF value of the cream increased with the concentration of hollow microspheres at an accelerating rate. Furthermore, sunscreens containing 15 wt% TX-85 as UV filters exhibited an SPF value of 10.73 ± 1.77. Replacing 5 wt% TX-85 with Cin-CNCs/$SiO_2$ hollow microspheres or Cin-CNCs/$TiO_2$ hollow microspheres in the same formulation increased the SPF values to 11.28 ± 1.86 and 13.41 ± 1.80, respectively. Thus, at the same UV filter concentration (15 wt%), these cinnamate-functionalized hollow microspheres significantly enhanced the UV protection performance of sunscreens.

Due to their high visible light transmittance, Cin-CNCs/$SiO_2$ hollow microspheres can reduce the whitening effect of sunscreens, while Cin-CNCs/$TiO_2$ hollow microspheres provide higher SPF values and broader UV-shielding capabilities. Therefore, in practical applications, different types of hollow microspheres can be selectively incorporated based on formulation requirements. Additionally, mixing $SiO_2$ and $TiO_2$ nanoparticles with Cin-CNCs to prepare hybrid hollow microspheres could balance their respective advantages, offering a versatile approach to optimizing sunscreen performance.

## 4. Conclusions

In this study, we present a novel method for fabricating hollow microspheres utilizing Cin-CNCs and inorganic nanoparticles ($SiO_2$ or $TiO_2$) *via* the Pickering emulsion templating approach. During the synthesis, the hydrolysis products of TEOS, Cin-CNCs, and $SiO_2$ nanoparticles synergistically stabilize the Pickering emulsion template. Unlike conventional organic UV filters, which pose potential risks and exhibit poor water solubility, these cinnamate-functionalized hollow microspheres (with an average size of approximately 1 μm) demonstrate excellent water dispersibility, superior photostability, and minimal skin absorption. Compared to inorganic UV filters, these hollow microspheres exhibit enhanced transparency and superior UV-shielding properties, attributed to the grafting of cinnamate groups and their unique hollow structure. When incorporated into sunscreen formulations, these hollow microspheres significantly improve the SPF performance compared to traditional inorganic UV filters, effectively combining the advantages of both organic and inorganic UV filters. The cinnamate groups exhibit strong absorption in the UVB region, while the hollow structure enhances the reflection and scattering of UV radiation. Additionally, the incorporation of $SiO_2$ or $TiO_2$ nanoparticles provides enhanced UVA protection and improves the mechanical properties of the hollow microspheres. These cinnamate-functionalized hollow microspheres not only deliver exceptional performance but also simplify sunscreen formulations by reducing the number of required organic components.

Looking forward, the potential scalability and economic feasibility of this approach are important considerations. The core materials employed, namely CNCs, $SiO_2$, and $TiO_2$ nanoparticles, are commercially available commodities. Furthermore, the Pickering emulsion templating process itself is inherently scalable and compatible with continuous flow systems, suggesting a viable pathway for larger-scale production.

## Author contributions

Fangyuan Ge: conceptualization, methodology, investigation, writing – original draft, and visualization. Man-hin Kwok: methodology and writing – reviewing & editing. To Ngai: writing – reviewing & editing, funding acquisition, project administration, and supervision.

## Conflicts of interest

There are no conflicts to declare.

## Data availability

The data supporting this article have been included as part of the supplementary information (SI). Supplementary information: FTIR, UV, calculation of grafting fractions of cinnamate groups, sample information, appearance photos, and sunscreen formulations for SPF testing. See DOI: **https://doi.org/10.1039/d5ma00509d**.

## Acknowledgements

The authors gratefully acknowledge the financial support provided by the Research Matching Grant Scheme at CUHK (Project No. 8601309).

## Notes and references

1 F. P. Gasparro, M. Mitchnick and J. F. Nash, *Photochem. Photobiol.*, 2008, **68**, 243–256.
2 A. C. Santos, J. Marto, R. Chá-Chá, A. M. Martins, M. Pereira-Silva, H. M. Ribeiro and F. Veiga, *Mater. Today Chem.*, 2022, **23**, 100709.
3 Y. Miao, Z. Tang, Q. Zhang, A. Reheman, H. Xiao, M. Zhang, K. Liu, L. Huang, L. Chen and H. Wu, *ACS Appl. Polym. Mater.*, 2022, **4**, 1448–1456.
4 N. Fleury, S. Geldenhuys and S. Gorman, *Int. J. Environ. Res. Public Health*, 2016, **13**, 999.
5 K. Geoffrey, A. N. Mwangi and S. M. Maru, *Saudi Pharm. J.*, 2019, **27**, 1009–1018.
6 J. D'Orazio, S. Jarrett, A. Amaro-Ortiz and T. Scott, *Int. J. Mol. Sci.*, 2013, **14**, 12222–12248.
7 O. P. Egambaram, S. Kesavan Pillai and S. S. Ray, *Photochem. Photobiol.*, 2020, **96**, 779–797.
8 L. T. Ngoc, V. V. Tran, J. Y. Moon, M. Chae, D. Park and Y. C. Lee, *Cosmetics*, 2019, **6**, 64.
9 A. A. Hodge, F. E. Hopkins, M. Saha and A. N. Jha, *Mar. Pollut. Bull.*, 2025, **213**, 117627.
10 A. Pniewska and U. Kalinowska-Lis, *Appl. Sci.*, 2024, **14**, 3302.
11 S. Tampucci, S. Burgalassi, P. Chetoni and D. Monti, *Cosmetics*, 2017, **5**(1), 1.
12 B. K. Amankwah, P. Sauer, K. Grabicova, P. C. von der Ohe, N. S. Ayikol and H. Kocour Kroupova, *J. Hazard. Mater.*, 2024, **471**, 134338.
13 N. Serpone, D. Dondi and A. Albini, *Inorg. Chim. Acta*, 2007, **360**, 794–802.
14 K. Morabito, N. C. Shapley, K. G. Steeley and A. Tripathi, *Int. J. Cosmet. Sci.*, 2011, **33**, 385–390.
15 A. C. Cozzi, P. Perugini and S. Gourion-Arsiquaud, *Eur. J. Pharm. Sci.*, 2018, **121**, 309–318.
16 T. H. Kim, S. H. Park, S. Lee, A. V. S. L. S. Bharadwaj, Y. S. Lee, C. G. Yoo and T. H. Kim, *Energies*, 2023, **16**, 2231.

17 N. R. Colas-Ruiz, M. G. Pintado-Herrera, M. Santonocito, B. Salerno, F. Tonini, P. A. Lara-Martin and M. Hampel, *Sci. Total Environ.*, 2024, **912**, 169178.
18 A. J. Conway, M. Gonsior, C. Clark, A. Heyes and C. L. Mitchelmore, *Sci. Total Environ.*, 2021, **796**, 148666.
19 C. Corinaldesi, F. Marcellini, E. Nepote, E. Damiani and R. Danovaro, *Sci. Total Environ.*, 2018, **637–638**, 1279–1285.
20 H. Yu, Z. Guo, S. Wang, G. S. N. Fernando, S. Channa, A. Kazlauciunas, D. P. Martin, S. A. Krasnikov, A. Kulak, C. Boesch and N. N. Sergeeva, *ACS Biomater. Sci. Eng.*, 2019, **5**, 2778–2785.
21 V. P. Chavda, D. Acharya, V. Hala, S. Daware and L. K. Vora, *J. Drug Delivery Sci. Technol.*, 2023, **86**, 104720.
22 T. Gracia-Cazana, J. Aguilera, A. Navarro-Bielsa, S. Gonzalez, H. W. Lim and Y. Gilaberte, *Photodermatol., Photoimmunol. Photomed.*, 2024, **40**, e12967.
23 M. D. Palm and M. N. O'Donoghue, *Dermatol. Ther.*, 2007, **20**, 360–376.
24 A. Jaroenworaluck, W. Sunsaneeyametha, N. Kosachan and R. Stevens, *Surf. Interface Anal.*, 2006, **38**, 473–477.
25 Z. Zhang, B. Zhang, N. Grishkewich, R. Berry and K. C. Tam, *Adv. Sustainable Syst.*, 2019, **3**, 1800156.
26 N. Heydari, A. R. Karimi, H. R. Momeni, F. Azadikhah and T. Etemadi, *ACS Omega*, 2025, **10**, 8250–8261.
27 Z. Zhang, K. C. Tam, X. Wang and G. Sèbe, *ACS Sustainable Chem. Eng.*, 2018, **6**, 2583–2590.
28 Y. Zhou, Y. Qian, J. Wang, X. Qiu and H. Zeng, *Biomacromolecules*, 2020, **21**, 3231–3241.
29 D. Bhattacharjee, *Int. J. Pharm. Res.*, 2021, **13**, 3494–3505.
30 N. Saewan and A. Jimtaisong, *J. Cosmet. Dermatol.*, 2015, **14**, 47–63.
31 A. Riya, A. Geeta, D. Gitika Arora and N. Manju, *Asian J. Pharm. Clin. Res.*, 2019, **12**, 7–15.
32 J. A. C. Nascimento Junior, A. M. Santos, A. M. S. Oliveira, A. B. Santos, A. A. de Souza Araujo, D. M. Aragon, L. A. Frank and M. R. Serafini, *AAPS PharmSciTech*, 2024, **25**, 212.
33 A. R. Hegde, M. U. Kunder, M. Narayanaswamy, S. Murugesan, S. C. Furtado, B. B. Veerabhadraiah and B. Srinivasan, *Environ. Sci. Pollut. Res. Int.*, 2024, **31**, 38061–38082.
34 S. M. Kandil, H. M. Diab, A. M. Mahfoz, A. Elhawatky and E. M. Abdou, *Pharm. Res.*, 2024, **41**, 1475–1491.
35 T. Foteva, *J. Chem. Technol. Metall.*, 2023, **59**, 3–14.
36 M. M. de Araujo, A. C. Schneid, M. S. Oliveira, S. V. Mussi, M. N. de Freitas, F. C. Carvalho, E. A. Bernes Junior, R. Faro and H. Azevedo, *Pharmaceutics*, 2024, **16**, 427.
37 J. Zhang, S. Zhang, C. Yan, J. Bi, X. Han and H. Liu, *ACS Appl. Nano Mater.*, 2024, **7**, 15365–15375.
38 D. J. Mendoza, M. Maliha, V. S. Raghuwanshi, C. Browne, L. M. M. Mouterde, G. P. Simon, F. Allais and G. Garnier, *Mater. Today Bio*, 2021, **12**, 100126.
39 N. A. Quatrano and J. G. Dinulos, *Curr. Opin. Pediatr.*, 2013, **25**, 122–129.
40 M. Syalsabilla, F. Sofaturahman, M. Syuriyani, L. R. Septiana, N. R. Aryani, R. Jonuarti, Ratnawulan and R. Hidayat, *Pillar Phys.*, 2023, **16**, 169–179.
41 P. Ataeian, Q. Shi, M. Ioannidis and K. C. Tam, *Carbohydr. Polym. Technol. Appl.*, 2022, **3**, 100201.
42 A. Rose, Z. Zhu, C. F. Madigan, T. M. Swager and V. Bulovic, *Nature*, 2005, **434**, 876–879.